optica

Universal multimode waveguide crossing based on transformation optics: supplementary material

SHUYI LI,[1] YANGYANG ZHOU,[2] JIANJI DONG,[1] XINLIANG ZHANG,[1] ERIC CASSAN,[3] JIN HOU,[4] CHUNYONG YANG,[4] SHAOPING CHEN,[4] DINGSHAN GAO,[1,5] AND HUANYANG CHEN[2,6]

[1]*Wuhan National Laboratory for Optoelectronics & School of Optical and Electronic Information, Huazhong University of Science and Technology, 1037 Luoyu Road, Wuhan 430074, China*

[2]*Institute of Electromagnetics and Acoustics and Department of Electronic Science, Xiamen University, Xiamen 361005, China*

[3]*Centre de Nanosciences et de Nanotechnologies, CNRS, Univ. Paris-Sud, Université Paris-Saclay, C2N-Orsay, 91405 Orsay cedex, France*

[4]*Hubei Key Laboratory of Intelligent Wireless Communications, College of Electronics and Information Engineering, South-Central University for Nationalities, Wuhan 430074, China.*

[5]*e-mail: dsgao@hust.edu.cn*

[6]*e-mail: kenyon@xmu.edu.cn*

Published 4 December 2018

This document provides supplementary information to "Universal multimode waveguide crossing based on transformation optics," https://doi.org/10.1364/OPTICA.5.001549. Sec. S1 provides the artificial boundary conformal mapping method used in the Article. Sec. S2 provides the method of converting the 2D graded index profile of transformed-fisheye multimode waveguide crossing (TF-MWC) to a 3D thickness profile. Sec. S3 describes the materials and fabrication methods of TF-MWC. Sec. S4 describes the measurement setup and auxiliary optical circuits on the same chip of TF-MWC. Sec. S5 gives and compares the simulation results of 5-channel 4-mode direct multimode waveguide crossing (D-MWC) and TF-MWC.

S1. ARTIFICIAL BOUNDARY CONFORMAL MAPPING WITH A SEMI-ANALYTIC FORM

In this section, we show how to obtain conformal mapping from Laplace's equation and how to optimize the shape of transformed sector ring to reach the following two goals. One is to maintain the index at the inner circular boundary unchanged. The other is to flatten the outer circular boundary and double the boundary index value.

We note that the original coordinates as (x, y), and the transformed coordinates as (u, v). In mathematics, a conformal mapping between this two sets of coordinates should obey the Cauchy-Riemann conditions [1, 2]

$$\frac{\partial u}{\partial x} = -\frac{\partial v}{\partial y}. \tag{S1}$$

$$\frac{\partial u}{\partial y} = \frac{\partial v}{\partial x}. \tag{S2}$$

After derivation, we can obtain the following Laplace's equations

$$\Delta u = 0. \tag{S3}$$

$$\Delta v = 0. \tag{S4}$$

In addition, we need to set the boundary conditions for these differential equations. The frequently used boundary conditions

are classified into two kinds. One is the Dirichlet condition with *u=constant*, which means a horizontal straight line. The other is the Neuman condition with $\partial u / \partial n = 0$, which represents a vertical straight line. Hence, the Laplace's equation method is generally applied for transforming a curved rectangle to a rectangle. In our design, the transformation belongs to this case. We can use the Laplace's equation module in COMSOL Multiphysics commercial software to easily solve it. But it should be noted that the boundary conditions cannot be set arbitrarily. Once the boundary conditions of *u* are set, the boundary conditions of *v* will be determined by the Cauchy-Riemann conditions.

The conformal mapping of the fisheye can be achieved by two steps. First, the original sector ring with inner radius R_{in} and outer radius R [Fig. S1(a)] is transformed to a rectangle [Fig. S1(b)]. This conformal mapping f_1 is obtained by solving the Laplace's equation on the original sector ring. And then the rectangle will be further transformed to the transformed sector ring [Fig. S1(c)]. For the convenience of setting boundary conditions, we solve its reverse transformation f_2 by applying the Laplace's equation on the transformed sector ring. The conformal mapping from original sector ring to the transformed sector ring is $f_2^{-1} \circ f_1$.

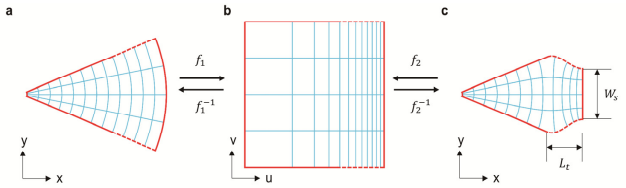

Fig. S1. The conformal mapping from original sector ring to the transformed sector ring, transited by a rectangle. (a) The original sector ring. (b) A rectangle as the intermediate transition. (c) The transformed sector ring. The original sector ring in panel (a) is transformed to the rectangle in panel (b) first. And then the rectangle is transformed to the transformed sector ring in panel (c). All the grids represent coordinates (u,v) in these objects, which are all presented in the polar coordinate form.

The conformal mapping f_1 could also be expressed by a complex analytic function $z = Aexp(mw)$, in which $z = x+iy$ and $w = u+iv$. We will use this function to obtain the boundary condition for *v* after setting boundary condition for *u*. For the original sector ring [Fig. S1(a)], we set the inner circle as $u = R_{in}$ and outer circle as $u = R$, which correspond to the left boundary and right boundary of the rectangle [Fig. S1(b)]. Considering this transformation, we know that the coordinates (R_{in}, 0) and (R, 0) are unchanged. The coefficients A and m can then be determined. After that, we could get the boundary conditions $v = -\theta / 2m$ and $v = \theta / 2m$ for the lower and upper boundaries of the original sector ring respectively, where θ represents the angle of the sector ring. The refractive index profile of the rectangle is then:

$$n_w = n_z \left| \frac{dz}{dw} \right| = \frac{n_0 mAR^2 \exp(mu)}{R^2 + A^2 \exp(2mu)}. \quad \textbf{(S5)}$$

For the transformed sector ring [Fig. S1(c)], the left boundary is a circular arc shared with the untransformed inner circle. The right boundary is a straight-line segment with width of W_s. The upper and lower boundaries are in mirror symmetry along the central x axis. They are both composed of two segments. One is a radial line from R_{in}=3 μm to R_{cut}. The other is a 3-order Bézier curve with horizontal length of L_t. We set the local coordinate origin at the beginning of this Bézier curve. And the expression for the Bézier curve on upper boundary is

$$y = p_0 x^3 + p_1 x^2 (L_t - x) + p_2 x (L_t - x)^2 + p_3 (L_t - x)^3. \quad \textbf{(S6)}$$

The parameters p_0, p_1, p_2 and p_3 can be expressed by W_s, R_{cut} and L_t, which are derived from the requirements of continuity and smoothness for the connection between the two segments. These three variables (W_s, R_{cut} and L_t) will then determine the shape of the transformed sector ring. We set them as the optimization parameters to reach the goal of index and wave front matching between TF-MWC and input/output waveguide. Once the shape of transformed sector ring is determined, by applying the same boundary conditions above mentioned to solve the Laplace's equations, we could get the second step of conformal mapping f_2.

The optimization objectives are set at two spatial points. One point is in the middle of the left circular boundary, on which the refractive index should remain unchanged after grid transformation. The other is in the middle of the right flat boundary, on which the refractive index should be doubled. We use the Bound Optimization BY Quadratic Approximation (BOBYQA) method in the COMSOL optimization module, and couple it with the Laplace's equation module. Once the three optimization variables vary, the Laplace's equation is solved repeatedly. Based on the calculated index changing ratio at the two points, the optimization module estimates the next values of the three optimization variables. When the two optimization objectives are both nearly achieved within a predefined threshold, the optimization process converges. Finally, we can obtain the optimal structural parameters R_{cut}= 16.9 μm, W_s= 8.77 μm and L_t= 6.05 μm for 4-channel 3-mode and R_{cut}= 22.0 μm, W_s= 9.97 μm and L_t= 8.90 μm for 5-channel 4-mode.

The second step of conformal mapping f_2 can also be in principle written in Taylor series:

$$w = \sum_k (a_k + ib_k) z^k. \quad \textbf{(S7)}$$

where we find that ten terms are already enough to obtain similar results. We show below the parameters in Table S1 and S2 for both 4-channel 3-mode and 5-channel 4-mode TF-MWCs.

Table S1 The parameters in Taylor series expression for the second step of conformal mapping in 4-channel 3-mode TF-MWC

k	a_k	b_k
0	-16.9	0.574
1	12.2	-0.650

2	-3.07	0.315
3	0.579	-0.0861
4	-0.0768	0.0148
5	0.00712	-0.00167
6	-0.000460	0.000126
7	1.99×10^{-5}	-6.27×10^{-6}
8	-5.58×10^{-7}	1.99×10^{-7}
9	9.10×10^{-9}	-3.63×10^{-9}
10	-6.56×10^{-11}	2.90×10^{-11}

Table S2 The parameters in Taylor series expression for the second step of conformal mapping in 5-channel 4-mode TF-MWC

k	a_k	b_k
0	-19.3	0.411
1	12.6	-0.382
2	-2.61	0.149
3	0.399	-0.0323
4	-0.0423	0.00433
5	0.00310	-0.000378
6	-0.000156	2.18×10^{-5}
7	5.27×10^{-6}	-8.28×10^{-7}
8	-1.14×10^{-7}	1.98×10^{-8}
9	1.44×10^{-9}	-2.72×10^{-10}
10	-7.93×10^{-12}	1.62×10^{-12}

S2. CONVERTING THE 2D GRADIENT INDEX PROFILE OF TF-MWC TO 3D THICKNESS PROFILE

In this section, we will show how to convert the 2D gradient index distribution of the transformed fisheye multimode waveguide crossing (TF-MWC) to the 3D thickness profile on the upper silicon layer of SOI wafer by effective index method [3].

If the silicon rectangle waveguide is wide enough, we could approximately use the scalar wave equations to describe the light field in the waveguide [3]. We assume light propagates along z direction. The x direction is perpendicular to the chip plane and pointing upward, so the y direction can be determined by the right-hand rule. For TE mode, the wave equation is

$$\nabla^2 E_y + k^2 n^2 E_y = 0. \quad \textbf{(S8)}$$

By separation of variables $E_y(x,y,z) = E_{y1}(x)E_{y2}(y,z)$, we can get two separated wave equations

$$\frac{\partial^2}{\partial x^2} E_{y1}(x) + k^2 (n^2 - n_{eff}^2) E_{y1}(x) = 0. \quad \textbf{(S9)}$$

$$\nabla_t^2 E_{y2}(y,z) + k^2 n_{eff}^2 E_{y2}(y,z) = 0. \quad \textbf{(S10)}$$

The Eq. (S9) is a mode eigenvalue equation of the slab waveguide. The Eq. (S10) describes a light wave propagating in the yz plane. The eigenvalue n_{eff} is the effective index of the slab waveguide, which is determined by the thickness of slab waveguide. Then the 2D gradient index profile of TF-MWC can be converted to a gradient thickness profile of slab waveguide. To realize this conversion, we need to calculate the effective indexes of the slab waveguides with different thickness values.

Our device is designed based on a commercial SOI wafer, which has 220 nm thick top silicon layer and 3 μm thick buried oxide layer. The upper cladding of waveguide is air. The material indexes of silicon and buried oxide at 1550 nm wavelength are 3.476 and 1.444 respectively. The sectional view of the silicon slab waveguide on SOI wafer is shown in Fig. S2(a), in which the silicon substrate is not shown. By solving Eq. (S9), the effective indexes of TE_0 mode of the silicon slab waveguides with different silicon thicknesses can be calculated and fitted to a curve, as shown in Fig. S2(b). From the fitted curve, we can translate the 2D gradient index of TF-MWC to the 3D thickness profile on the upper silicon layer of SOI wafer.

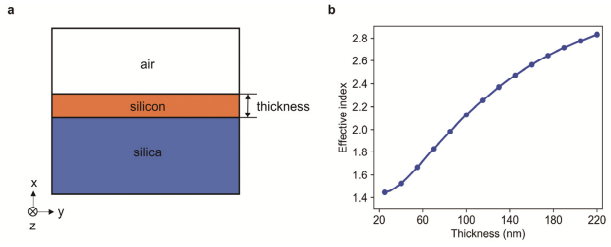

Fig. S2. The silicon slab waveguide and its effective index in different thickness. (a) The sectional view of the silicon slab waveguide on SOI wafer, which has 220 nm thick top silicon layer and 3 μm thick buried oxide layer. (b) The relation between the TE_0 mode effective index for the silicon slab waveguide and the thickness of the upper silicon layer. The circular dots are calculated values and the solid line is the fitted curve.

S3. MATERIALS AND FABRICATION METHODS

We used grayscale E-beam lithography to fabricated the TF-MWC in this work. The polymethyl methacrylate (PMMA) 950k resist (Allresist, AR-P 679.04, 4%) is used for the grayscale E-beam lithography. First, 400 nm thick PMMA 950k resist was spin coated on SOI wafer (SOITEC, Unibound, 220 nm top silicon layer, 3 μm buried oxide layer) at 2000 rpm for 60 s. Then the 3D profile of TF-MWC was written on the resist by grayscale E-beam lithography (Vistec, EBPG 5000+). After E-beam lithography, the resist was developed in a mixture of isopropyl alcohol (IPA) and deionized water in proportion 2:1 for 20 s. The E-beam exposure dose before proximity effect correction (PEC) is varied from 300 μC/cm² to 540 μC/cm², resulting in an exponentially distributed resist thicknesses from 60 nm to 400 nm after development. To reduce the resist roughness, we reflowed the PMMA resist for 10 min at 120 ℃ on a hot plate. Then an inductively-coupled plasma (ICP) etching for 50 s was followed to transfer the 3D profile patterned on resist to the upper silicon layer of SOI wafer. The thickness profile transferring scaling factor can be obtained in advance by measuring the etch rate ratio between silicon and PMMA resist.

S4. THE MEASUREMENT SETUP AND THE AUXILIARY CIRCUITS

In this section, we present the measurement setup and the auxiliary circuits on the chip.

The measurement setup is shown in Fig. S3. A wideband amplified spontaneous emission (ASE) light source covering the C and L bands is used in our measurement. The continuous-wave (CW) ASE light is passed through a polarization controller (PC) to tune the polarization to TE. Then the light is coupled in and out of the fabricated chip vertically with single-mode fibers by the input and output grating couplers on-chip. After the output fiber, a commercial 3 dB Y-splitter is connected to split the output light into two paths. One is linked to the optical power meter for monitoring and tuning the alignment between the single-mode fibers and the grating couplers. The other is connected to the optical spectrum analyzer (OSA) to measure the efficiency spectra for every mode and every crossing channel.

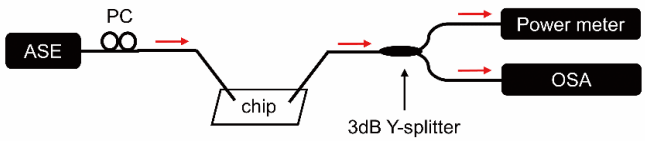

Fig. S3. The measurement setup. The light from C+L band amplified spontaneous emission (ASE) source is passed through a polarization controller (PC) and coupled in and out of the chip with single-mode fibers by on-chip grating couplers. After the output fiber, a commercial 3 dB Y-splitter is connected to split the output light into two paths. One is linked to the optical power meter for monitoring and tuning the alignment between the single-mode fibers and the grating couplers. The other is connected to the optical spectrum analyzer (OSA) to measure the efficiency spectra for every mode and every crossing channel.

Besides the TF-MWC, several auxiliary circuits including independent straight waveguides, mode multiplexers and de-multiplexers and D-MWC were also fabricated on the same chip. Figure S4 shows the circuit of D-MWC. It has the same structure with the TF-MWC except the crossing region. Figure S4(c) shows the magnified microscopic view of the crossing region of D-MWC. The mode multiplexers/de-multiplexers [Fig. S4(d)] and grating couplers [Fig. S4(e)] in the D-MWC are identical to those in the TF-MWC. It can be then a comparison between the performance of D-MWC and TF-MWC. To obtain the energy transmission efficiency for every mode at every port, we needed to subtract the loss of mode multiplexing system (including back to back mode multiplexer and de-multiplexer) from the measured spectrum. Considering the possible fabrication non-uniformity in different channel direction, we fabricated the referenced multimode multiplexing systems in all the four channel directions, such as the horizontal direction [Fig. S4(h)], the vertical direction [Fig. S4(c)], the anti-oblique direction [Fig. S4(b)] and the oblique direction [Fig. S4(e)]. And we finally obtained the transmission efficiency for every mode in every channel direction by subtracting the loss of the corresponding referenced multimode multiplexing system.

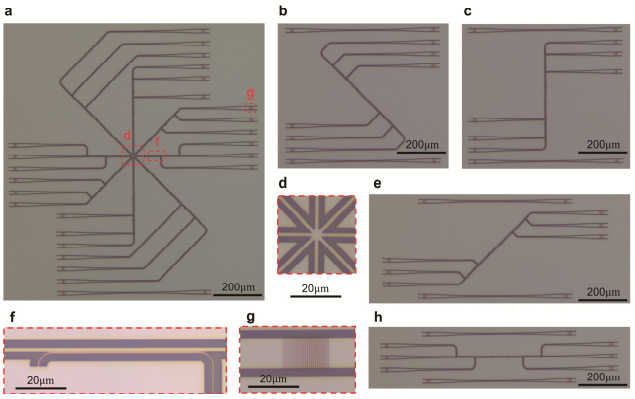

Fig. S4. The auxiliary circuits on the same chip. (a) The circuit of the D-MWC for comparing with the TF-MWC. (b,c,e,h) The reference mode multiplexing systems in horizontal direction (h), vertical direction (c), anti-oblique direction (b) and oblique direction (e). (d) The magnified microscopic view of the D-MWC. (f) The asymmetrical directional coupler (ADC) structure of the mode multiplexer/demultiplexer. (g) The grating coupler for coupling the light between the single mode fiber and the circuit on chip.

S5. THE SIMULATION RESULTS OF 5-CHANNEL 4-MODE D-MWC AND TF-MWC

In this section, we present the simulation results of 5-channle 4-mode D-MWC and TF-MWC by 3D FDTD method.

To show the advantage of our proposed TF-MWC, we also simulate a 5-channel 4-mode direct multimode waveguide crossing (D-MWC) for comparison. For supporting lowest four TE modes from the wavelength 1.1~2.0 μm, we widen the input multimode waveguide to 3 μm. The simulated efficiency holographs and propagation field diagrams for 1550 nm wavelength are shown in Figs. S5 and S6 respectively. For TE_0, TE_1, TE_2 and TE_3 modes, the transmission efficiencies are 79.2% (-1.01 dB), 30.0% (-5.23 dB), 3.3% (-14.85 dB) and 1.3% (-18.85 dB) respectively. The maximum crosstalks are -11.12 dB, -6.00 dB, 7.33 dB and 11.40 dB respectively. To display the simulation results clearly, we plot four histograms for four different input modes respectively. In each histogram, the energy efficiency of every mode in every port is listed. The through port is noted as port T. For simplicity, we number the remaining four crossing ports from C1 to C4 in counterclockwise order. As shown in the results, we could find the losses and crosstalks deteriorate obviously for higher order modes. Especially for TE_2 and TE_3 mode, the crosstalks to port C1 are even higher than the corresponding transmission efficiencies. This is caused by the strong diffraction and scattering when light propagates through the crossing, as shown in Fig. S6, which is similar to the case of 4-channle 3-mode D-MWC.

For the 5-channel 4-mode TF-MWC, the 3D FDTD simulation results for 1550 nm wavelength are shown in figures S7 and S8. For TE_0, TE_1, TE_2 and TE_3 modes, the transmission efficiencies are 99.6% (-0.02 dB), 98.6% (-0.06 dB), 96.0% (-0.18 dB) and 93.1% (-0.31 dB) respectively. The maximum crosstalks are -42.57 dB, -

37.46 dB, -41.68 dB and -36.07 dB respectively. So the crosstalks to other ports or to other modes are below -36 dB. From Fig. S8, one can see that all the four modes can be adiabatically varied and recovered through the TF-MWC. Hence, the simulation results prove that the proposed 5-channel 4-mode waveguide star crossing has very high transmission efficiencies and low crosstalks for the lowest four TE modes.

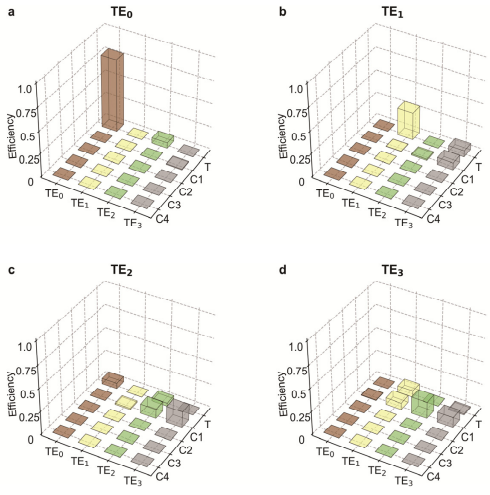

Fig. S5. The energy efficiencies of the lowest four order TE modes in the 5-channel 4-mode direct multimode waveguide crossing (D-MWC), simulated by 3D FDTD. (a-d) Efficiency histograms of TE_0 (a), TE_1 (b), TE_2 (c) and TE_3 (d) mode propagations at 1550 nm wavelength are shown respectively. And the width of every multimode waveguide is 3 μm. The label T represents the throughout port. The labels C1 to C4 denote the crossing ports respectively in counterclockwise order.

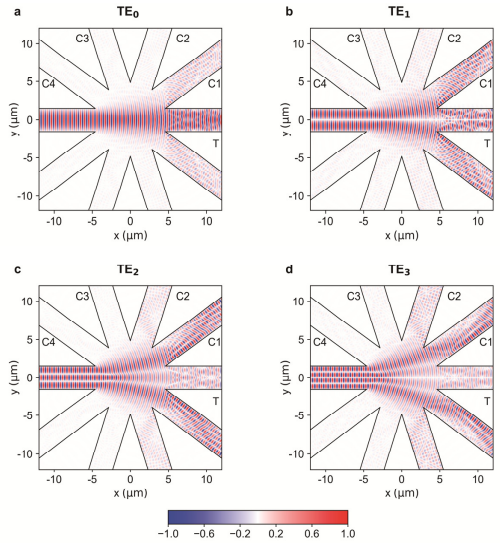

Fig. S6. The propagation of the lowest four order TE modes in the 5-channel 4-mode direct multimode waveguide crossing (D-MWC), simulated by 3D FDTD. (a-d) The profiles of the H_z field component for TE_0 (a), TE_1 (b), TE_2 (c) and TE_3 (d) modes at 1550 nm wavelength. And the width of every multimode waveguide is 3 μm. The label T represents the throughout port. The labels C1 to C4 denote the crossing ports respectively in counterclockwise order.

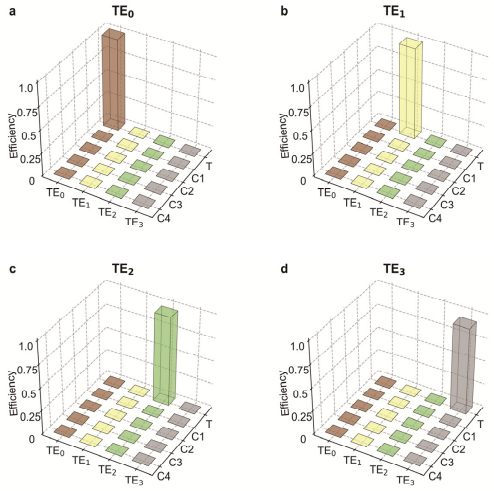

Fig. S7. The energy efficiencies of the lowest four order TE modes in the 5-channel 4-mode transformed fisheye multimode waveguide crossing (TF-MWC), simulated by 3D FDTD. (a-d) Efficiency histograms of TE_0 (a), TE_1 (b), TE_2 (c) and TE_3 (d) mode propagations at 1550 nm wavelength are shown respectively. And the waveguide width is 3 μm. The labels are the same as those in Fig. S5. Simulation results show that the through port efficiencies of all lowest four order TE modes are above 93.1% (-0.31 dB) and crosstalks to other modes or other ports are below -36 dB.

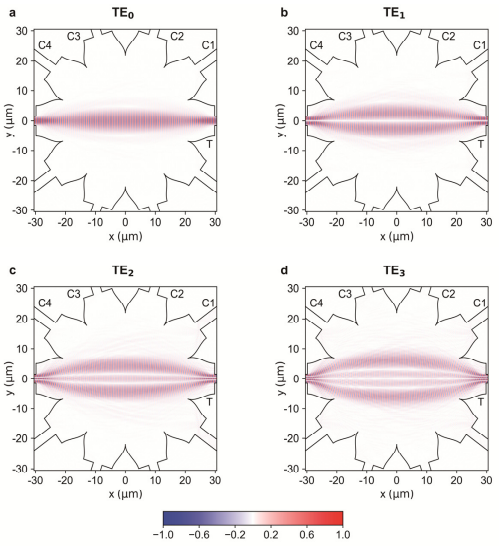

Fig. S8. The propagation of the lowest four order TE modes in the 5-channel 4-mode transformed fisheye multimode waveguide crossing (TF-MWC), simulated by 3D FDTD. (a-d) The profiles of the H_z field component for TE_0 (a), TE_1 (b), TE_2 (c) and TE_3 (d). And the waveguide width is 3 μm. The labels are the same as those in Fig. S6.

The theoretical spectra of the 5-channel 4-mode TF-MWC for TE_0, TE_1, TE_2 and TE_3 modes are shown in Figs. S9 (a0, a1, a2, a3) respectively. And Figs. S9 (b0, b1, b2, b3) are the spectra of the 5-channel 4-mode D-MWC for TE_0, TE_1, TE_2 and TE_3 modes respectively. From these diagrams, we can find the D-MWC has large losses and serious crosstalks, especially for the propagations of higher order modes. In contrast, for TF-MWC, throughout a broad wavelength range of 1241~1720 nm, the losses of all modes are below -1.20 dB and the crosstalks are all below -17 dB.

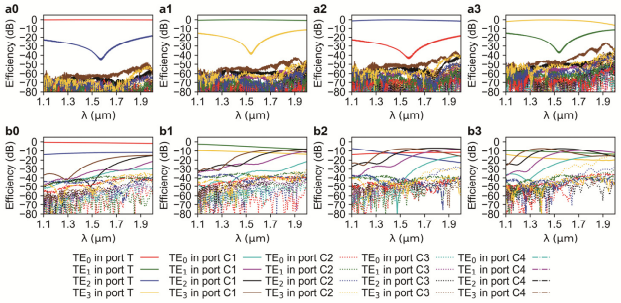

Fig. S9. The calculated spectra of the 5-channel 4-mode transformed fisheye multimode waveguide crossing (TF-MWC) and direct multimode waveguide crossing (D-MWC) by the 3D FDTD simulation. (a0-a3) The theoretical spectra of TF-MWC for TE_0 (a0), TE_1 (a1), TE_2 (a2) and TE_3 (a3) modes respectively. (b0-b3) The theoretical spectra of the D-MWC for TE_0 (b0), TE_1 (b1), TE_2 (b2) and TE_3 (b3) modes respectively.

References

1. Y. G. Ma, N. Wang, and C. K. Ong, "Application of inverse, strict conformal transformation to design waveguide devices," J. Opt. Soc. Am. A. Opt. Image. Sci. Vis. **27**, 968-972 (2010).
2. N. I. Landy and W. J. Padilla, "Guiding light with conformal transformations," Opt. Express **17**, 14872-14879 (2009).
3. A. Boudrioua, *Photonic waveguides: theory and application* (ISTE Ltd, John Wiley & Sons, Inc., London SW19 4 EU, Hoboken, NJ 07030, 2013), p. 30.